Three-dimensional unsteady model of arc heater plasma flow

Jeremie B.E. Meurisse, Alejandro Alvarez Laguna, Marco Panesi, Nagi Mansour

Three-dimensional unsteady model of arc heater plasma flow

Jeremie B. E. Meurisse[a,*], Alejandro Alvarez Laguna[b], Marco Panesi[c], Nagi N. Mansour[a]

[a] *Analytical Mechanics Associates, Inc. at NASA Ames Research Center, Moffett Field, CA 94035, USA*
[b] *Laboratoire de Physique des Plasmas (LPP), CNRS, Observatoire de Paris, Sorbonne Université, Université Paris Saclay, Ecole polytechnique, Institut Polytechnique de Paris, 91120 Palaiseau, France*
[c] *University of Illinois at Urbana-Champaign, Champaign, IL, USA*

Abstract

Arc jets are unique facilities used to evaluate the performance of Thermal Protection Systems (TPS) for hypersonic vehicles. They produce high pressure and high enthalpy plasma flow to simulate the extreme heat encountered during atmospheric entry. The constricted arc heater part of an arc jet increases the test gas temperature by Joule heating. This study details the development of the three-dimensional unsteady plasma flow analysis tool, ARCHeS (ARC Heater Simulator). Coupled Navier-Stokes, radiative transfer and Maxwell equations yield current density, magnetism, radiation, and flow field solutions. The present work constitutes the first demonstration of an unsteady three-dimensional plasma flow simulation of high pressure and high enthalpy arc heater that captures kink instabilities of the electric arc. It is found that the arc attachment is mainly driven by upstream arc instabilities.

Keywords: Arc jet, Arc heater, Radiative transfer, Joule heating, Plasma, Arc instability, Arc attachment.

*Corresponding author
Email address: jeremie.b.meurisse@nasa.gov (Jeremie B. E. Meurisse)
Preprint submitted to Aerospace Science and Technology
November 14, 2022

Nomenclature

$\mathcal{I}_\nu^d$	Discrete radiative intensity in direction $\boldsymbol{\Omega}^d$, $\mathrm{W} \cdot \mathrm{m}^{-2}$
$\mathcal{I}_\nu$	Radiative intensity, $\mathrm{W} \cdot \mathrm{m}^{-2} \cdot \mathrm{sr}^{-1}$
$\boldsymbol{A}$	Magnetic vector potential, $\mathrm{T} \cdot \mathrm{m}$
$\boldsymbol{B}$	Magnetic field, T
$\boldsymbol{E}$	Electric field, $\mathrm{V} \cdot \mathrm{m}^{-1}$
$\boldsymbol{J}$	Current density, $\mathrm{A} \cdot \mathrm{m}^{-2}$
$\boldsymbol{n}$	Normal direction
$\boldsymbol{q}$	Heat flux, $\mathrm{W} \cdot \mathrm{m}^{-2}$
$\boldsymbol{t}$	Tangential direction
$\boldsymbol{u}$	Velocity, $\mathrm{m} \cdot \mathrm{s}^{-1}$
$\mathcal{H}$	Planck's constant, $\mathrm{kg} \cdot \mathrm{m}^2 \cdot \mathrm{s}^{-1}$
$\dot{m}$	Mass flux, $\mathrm{kg} \cdot \mathrm{s}^{-1}$
$\mathbf{S}$	Outgoing surface normal, m^2
a_d	Gaussian quadrature weight
B_ν	Banded black body spectral radiative intensity, $\mathrm{W} \cdot \mathrm{m}^{-2}$
c	Speed of light in the medium., $\mathrm{m} \cdot \mathrm{s}^{-1}$
e	Internal energy, $\mathrm{J} \cdot \mathrm{kg}^{-1}$
E_0	Stagnation energy, $\mathrm{J} \cdot \mathrm{kg}^{-1}$
h	Enthalpy, $\mathrm{J} \cdot \mathrm{kg}^{-1}$
H_0	Stagnation enthalpy, $\mathrm{J} \cdot \mathrm{kg}^{-1}$
I	Electric current, A
k_B	Boltzmann's constant, $\mathrm{J} \cdot \mathrm{K}^{-1}$
k_i	Incoming part of the radiative directional split
k_o	Outgoing part of the radiative directional split
L_0	Characteristic length, m
M	Mach number
N_a	Number of anodes
N_b	Number of spectral bands
N_d	Number of directions

p	Pressure, Pa
Q_J	Joule heating, $\mathrm{W} \cdot \mathrm{m}^{-3}$
R_b	Resistance of the ballast configuration, Ω
Re_m	Magnetic Reynolds number
S	Surface area, m^2
T	Temperature, K
U_0	Characteristic velocity, $\mathrm{m} \cdot \mathrm{s}^{-1}$
V	Volume, m^3

Greek

$\mathbf{\Omega}^d$	Discrete direction
α	Diffusivity, $\mathrm{kg} \cdot \mathrm{m}^{-1} \cdot \mathrm{s}^{-1}$
$\boldsymbol{\omega}$	Vorticity, s^{-1}
$\underline{\underline{\boldsymbol{\tau}}}$	Viscous stress tensor, $\mathrm{kg} \cdot \mathrm{m} \cdot \mathrm{s}^{-2}$
ϵ_ν	Emissivity
η	Magnetic diffusivity, $\mathrm{m}^2 \cdot \mathrm{s}^{-1}$
γ	Heat capacity ratio
κ_ν	Linear absorption coefficient, m^{-1}
μ	Mixture viscosity, $\mathrm{kg} \cdot \mathrm{m}^{-1} \cdot \mathrm{s}^{-1}$
μ_0	Vacuum magnetic permeability, $\mathrm{H} \cdot \mathrm{m}^{-1}$
ϕ	Electric potential, V
ψ	Compressibility, $\mathrm{s}^2 \cdot \mathrm{m}^{-2}$
ρ	Mass density, $\mathrm{kg} \cdot \mathrm{m}^{-3}$
σ	Electrical conductivity, $\mathrm{S} \cdot \mathrm{m}^{-1}$

Subscripts

w	Wall
e	External
imp	Imposed
ind	Induced
a	Anodes
b	Spectral band

c	Cathodes
nc	Neighbor cell
tot	Total

Superscripts

cond	Conductive
d	Direction
rad	Radiative

1. Introduction

High enthalpy arc jet wind tunnels are the established ground-test technology used to evaluate the performance of Thermal Protection Systems (TPS) materials for human and robotic exploration missions. By providing a highly energetic flow over prolonged test times, arc jet facilities enable testing materials under extreme aerothermal heating experienced by spacecraft during planetary entry.

Arc jets are usually composed of an anode chamber, a long constrictor, a cathode chamber, a converging/diverging nozzle, and a test chamber. The number of electrodes, commonly made of copper, around the anode and cathode chambers is different among arc jet facilities. The large difference in electric potential between the anodes and the cathodes generates the extreme current necessary to heat the test gas via Joule heating. The electrodes and the walls have an internal water-cooling system to remove the heat created by the electric arc. The constrictor, where most of the heating occurs, is usually built as a succession of gas-injecting disks that are insulated from each other by a ceramic material. The mixture of the cold gas injected through the disks is representative of the planetary atmosphere of interest to a test campaign. This study focuses on the arc heater part of an arc jet from the anode chamber to the nozzle throat.

Although the supersonic aerothermal modeling technology from the nozzle throat to the test chamber is well established and routinely used, the inlet conditions from the arc heater section have always been highly approximated in the literature [28, 6, 15]. An accurate model of the plasma physics that occur in the arc heater is needed to understand the gas conditions at the nozzle throat. High fidelity heat and mass transfer analysis tools of the sample material response in the test chamber are an active area of research [26, 3, 23, 8].

The importance of understanding the arc attachment and arc instabilities in arc jets was studied by [2, 36]. The interaction between the electric arc and the surrounding medium results in strong gradients in both the fluid and the electromagnetic fields, which can lead to various types of instabilities [5].

Numerical methods to compute the radiative transfer are available in the literature, such as ray tracing [48, 20, 22] and spatial and spectral discretization [4, 25, 24, 1]. Research by Trelles et al. [40, 37, 38, 39] investigated finite element modeling of industrial arc plasma torches using Argon gas. The collection of work by Trelles et al. includes detailed models of the plasma. However, given the empirical nature of the radiation model used, this work is more suitable for smaller geometries, and lower total enthalpy flows. Park et al. [27], Sakai et al. [32, 31, 33, 30], and Lee et al. [19, 18] have studied numerical models of plasma flow in arc heaters. Wang et al. [44, 42, 43] have worked on modeling 3D vacuum arcs used in industrial applications, such as circuit breakers. Some of their results have been compared to anode jet experimental data. A three-dimensional unsteady simulation of NASA's Aerodynamic Heating Facility was performed by Sahai et al. [29] using the Fully-Implicit Navier-Stokes (FIN-S) solver [16, 17]. Their finite element solver included Joule heating, 3D radiative transfer, and non-equilibrium model for the plasma. A simplified geometry was used for the anode and cathode chambers in their study. The computational cost of the solver limited the integration in time.

The objective of this study is to develop a better understanding of the multi-physics of the plasma flow inside arc heaters which will ultimately lead to a more accurate characterization of the use of an arc jet in testing TPS materials. The state-of-the-art ARC Heater Simulator (ARCHeS) analysis tool provides a parallel, unstructured, finite volume solver based on the OpenFOAM library. ARCHeS includes the solution of three-dimensional radiative transfer, imposed current density, imposed magnetic field, external magnetic field, and turbulence. Realistic boundary conditions are added to the model. The open-source third party library Mutation++, developed at the von Karman Institute for Fluid Dynamics, is used to compute the equilibrium gas mixture composition as well as thermodynamic and transport properties [35]. Three-dimensional and time-dependent simulations presented in this work show plasma instabilities in the constrictor of the arc heater. Analysis of the electric arc dynamics will provide a better intuitive understanding of the complex behavior of plasma flow observed

in arc jets. Massively parallel and efficient simulation capability in ARCHeS allows long-time integration, necessary for the development of the plasma instabilities.

The paper is organized as follows. In section 2, the governing equations and the boundary conditions used in the plasma flow model are presented. Section 3 details the numerical model applied to solve the governing equations. In section 4, overall results are presented, including arc instabilities and attachment. Finally, section 5 summarizes the conclusions drawn from this study.

2. Governing Equations

2.1. Mass, momentum, and energy equations

The governing equations, described in Eq. (1), are the mass, momentum, and energy conservation laws.

$$\partial_t \rho + \boldsymbol{\partial_x} \cdot (\rho \boldsymbol{u}) = 0 \tag{1a}$$

$$\partial_t (\rho \boldsymbol{u}) + \boldsymbol{\partial_x} \cdot (\rho \boldsymbol{u}\boldsymbol{u}) = -\boldsymbol{\partial_x} p + \boldsymbol{\partial_x} \cdot \underline{\underline{\boldsymbol{\tau}}} + \boldsymbol{J} \times \boldsymbol{B} \tag{1b}$$

$$\partial_t (\rho E_0) + \boldsymbol{\partial_x} \cdot (\rho H_0 \boldsymbol{u}) = \boldsymbol{\partial_x} \cdot (\underline{\underline{\boldsymbol{\tau}}} \cdot \boldsymbol{u} - \boldsymbol{q}^{cond}) + \sigma |\boldsymbol{E}|^2 + \boldsymbol{u} \cdot (\boldsymbol{J} \times \boldsymbol{B}) - \boldsymbol{\partial_x} \cdot \boldsymbol{q}^{rad} \tag{1c}$$

H_0, E_0 and e are the stagnation enthalpy, stagnation energy, and internal energy.

$$H_0 = E_0 + \frac{p}{\rho} = e + \frac{|\boldsymbol{u}|^2}{2} + \frac{p}{\rho} \tag{2}$$

The Lorentz force and work, the Joule heating, and the radiative heating/cooling are detailed in the following subsections.

2.2. Electromagnetic equations

Chapter 3.4 of Goedbloed & Poedts [12] and section 5 of Giordano [10] give a general review of the coupling between plasma and Maxwell's equations. The governing equations, detailed in Eq. (1), remain unclosed. Maxwell's equations

result in the following dynamic equations for the current and magnetic fields. Ampere's law is given by

$$-\frac{1}{c^2}\partial_t \boldsymbol{E} + \boldsymbol{\partial}_x \times \boldsymbol{B} = \mu_0 \boldsymbol{J} \tag{3}$$

Given the non-relativistic system in the arc heater ($U_0 << c^2$), Ampere's law, Eq. (3), reduces to

$$\boldsymbol{\partial}_x \times \boldsymbol{B} = \mu_0 \boldsymbol{J} \tag{4}$$

The generalized Ohm's law, as shown in Eq. (40) of Ref. [10], is given by

$$\boldsymbol{J} = \sigma \left(\boldsymbol{E} + \boldsymbol{u} \times \boldsymbol{B} \right) \tag{5}$$

The magnetic Reynolds number, detailed in Eq. (6), compares magnetic induction to magnetic diffusion.

$$Re_m = \frac{U_0 L_0}{\eta} \tag{6a}$$

$$\eta = \frac{1}{\mu_0 \sigma} \tag{6b}$$

In the considered arc heaters, the magnetic Reynolds number is about 10^{-3}, which corresponds to a highly resistive plasma. This system with low Re_m is dominated by magnetic diffusion, and inductive terms are neglected. Using the quasi-static approximation, the Ohm's law, from Eq. (5), reduces to

$$\boldsymbol{J} = \sigma \boldsymbol{E} \tag{7}$$

In this work, the electromagnetic four-potential formulation [14] is used to write

$$\boldsymbol{E} = -\boldsymbol{\partial_x} \phi - \partial_t \boldsymbol{A} \tag{8a}$$

$$\boldsymbol{B} = \boldsymbol{\partial_x} \times \boldsymbol{A} \tag{8b}$$

In this case, the current is driven by a differential of electric potential between the electrodes, and an external magnetic field in the electrode region is added to prevent the arc attachment at one point. The total electric field is split into two parts in order to simplify the boundary conditions. The first part is an imposed electric field, $\boldsymbol{E}_{imp}$, where the fluid is assumed stationary compared to the imposed electric potential. Therefore, the fluid is treated as an electric conductor. The second part is an induced electric field, $\boldsymbol{E}_{ind}$, generated by fluctuations of the total magnetic vector potential and the gradient of the induced electric potential. The split of the total electric field follows

$$\boldsymbol{E}_{imp} = -\boldsymbol{\partial}_{\boldsymbol{x}}\phi_{imp} \tag{9a}$$

$$\boldsymbol{E}_{ind} = -\partial_t(\boldsymbol{A}_{imp} + \boldsymbol{A}_e + \boldsymbol{A}_{ind}) - \boldsymbol{\partial}_{\boldsymbol{x}}\phi_{ind} \tag{9b}$$

$$\boldsymbol{E} = \boldsymbol{E}_{imp} + \boldsymbol{E}_{ind} \tag{9c}$$

Ohm's law, from Eq. (7), yields

$$\boldsymbol{J}_{imp} = -\sigma\boldsymbol{\partial}_{\boldsymbol{x}}\phi_{imp} \tag{10a}$$

$$\boldsymbol{J}_{ind} = -\sigma\left[\partial_t(\boldsymbol{A}_{imp} + \boldsymbol{A}_e + \boldsymbol{A}_{ind}) + \boldsymbol{\partial}_{\boldsymbol{x}}\phi_{ind}\right] \tag{10b}$$

$$\boldsymbol{J} = \boldsymbol{J}_{imp} + \boldsymbol{J}_{ind} \tag{10c}$$

The induced fields generated by the movement of the charges in the plasma flow were not computed in this work. As shown in Eq. (6), the low magnetic Reynolds number indicates that advection is relatively unimportant, which means that the electric field ($\boldsymbol{E}$) is determined by the boundary conditions ($\boldsymbol{E}_{imp}$) rather than the flow ($\boldsymbol{E}_{ind}$). Therefore, the induced electric field and the magnetic vector potential were neglected. Future work will compare the

induced and imposed fields.

$$\boldsymbol{E}_{ind} = \boldsymbol{A}_{ind} = \boldsymbol{0} \tag{11}$$

2.2.1. Imposed electric field

We define the imposed electric field as the electric field that is created by the potential difference between the electrodes. The electric field is sustained inside the plasma due to the finite conductivity, which generates a conductive current that heats the gas. Consequently, the imposed current continuity comes from the divergence of Eq. (4) that yields the current conservation relation,

$$\boldsymbol{\partial_x} \cdot \boldsymbol{J}_{imp} = 0. \tag{12}$$

The plasma is considered to be quasi-neutral in the whole domain, hence neglecting the sheaths at the walls and electrodes.

Substituting Eq. (10a) in Eq. (12) gives

$$\boldsymbol{\partial_x} \cdot (-\sigma \boldsymbol{\partial_x} \phi_{imp}) = 0 \tag{13}$$

By solving for the electric potential using Eq. (13), the electric field is computed as

$$\boldsymbol{E}_{imp} = -\boldsymbol{\partial_x} \phi_{imp} \tag{14}$$

The Joule heating is expressed as follows

$$Q_J = \sigma |\boldsymbol{E}_{imp}|^2 = \sigma | - \boldsymbol{\partial_x} \phi_{imp}|^2 \tag{15}$$

2.2.2. Imposed magnetic field

The imposed magnetic field is defined as the magnetic field induced by the imposed current. Using charge neutrality of the plasma, the imposed vector

magnetic field must satisfy,

$$-\partial_x^2 \boldsymbol{A}_{imp} = -\mu_0 \sigma \boldsymbol{\partial_x} \phi_{imp} \tag{16}$$

After solving for the imposed magnetic vector potential using Eq. (16), the imposed magnetic field is computed as follows,

$$\boldsymbol{B}_{imp} = \boldsymbol{\partial_x} \times \boldsymbol{A}_{imp} \tag{17}$$

This ensures that $\boldsymbol{\partial_x} \cdot \boldsymbol{B}_{imp} = 0$. Note that in regions where the flow is not conductive, i.e., $\sigma \approx 0$, the imposed magnetic vector potential satisfies the Laplace equation.

$$\partial_x^2 \boldsymbol{A}_{imp} \approx 0 \tag{18}$$

2.2.3. External magnetic field

The external magnetic field is the magnetic field that is generated outside the plasma by an external source. In the studied arc heaters, a magnetic field is created within the electrode to create a force that moves the attachment point of the current and protects the electrode from erosion [46], as represented in Fig. 1.

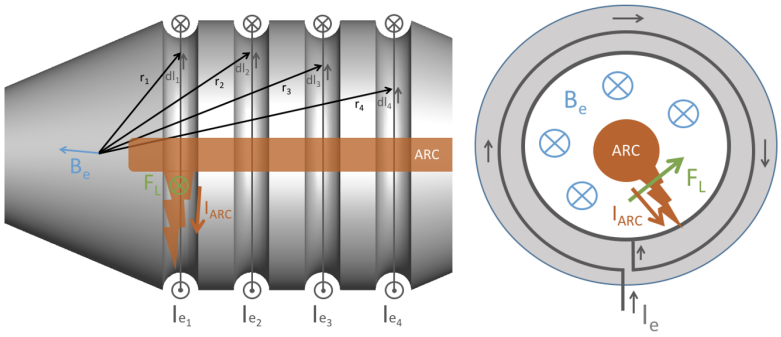

Figure 1: Representation of the magnetic spin coil in series with the arc current contained in each electrode. The external magnetic field creates a force that rotates the arc attachment point and reduces erosion.

The Biot-Savart law is used to express the external magnetic field $\boldsymbol{B}_e$, generated by the wire wrapped within the electrode assembly,

$$\partial_x^2 \boldsymbol{A}_e = -\mu_0 \boldsymbol{J}_e \tag{19}$$

The analytic solution of Eq. (19) is given by

$$\boldsymbol{A}_e(\boldsymbol{r}) = \frac{\mu_0}{4\pi} \int \frac{\boldsymbol{J}_e(\boldsymbol{r'})}{|\boldsymbol{r} - \boldsymbol{r'}|} d^3\boldsymbol{r'} \tag{20}$$

For a thin wire of infinitesimal thickness, this results in

$$\boldsymbol{A}_e(\boldsymbol{r}) = \frac{\mu_0 I_e}{4\pi} \oint \frac{\boldsymbol{dl}}{|\boldsymbol{r} - \boldsymbol{r'}|} \tag{21}$$

where $\oint$ is the integral along the length of the wire. The external magnetic vector potential from Eq. (21) was numerically solved using 60 points for the contour integral. The external magnetic field was then computed as follows

$$\boldsymbol{B}_e = \boldsymbol{\partial_x} \times \boldsymbol{A}_e \tag{22}$$

This formulation ensures that $\boldsymbol{\partial_x} \cdot \boldsymbol{B}_e = 0$ in the computational domain.

2.3. Radiative heat flux

Radiative Transfer Equations (RTE) are solved in this work to characterize the radiative heat flux. In the literature on arc plasma torches modeling, simpler approaches are found to tackle radiation. The most common one considers the radiative flux as a function of the local properties through a Net Emission Coefficient (NEC) [21, 11]. Alternatively, the tangent slab approximation that reduces the RTE to one spatial dimension is often used for cylindrical geometries [34]. However, both approximations cannot be used in the presence of 3D instabilities with strong temperature gradients, as the radiation no longer depends on the local properties nor the physics can be reduced to cylindrical symmetry.

The total radiative heat flux is given by integrating the spectral radiative heat flux over the entire spectrum. The integral is approximated by a sum of

discrete spectral radiative heat fluxes with a number of bands N_b, as follows,

$$\mathbf{q}^{rad} \approx \sum_{\nu=1}^{N_b} \mathbf{q}_\nu^{rad} \tag{23}$$

Here, $\mathbf{q}_\nu^{rad}$ is given by integrating the radiative intensity in direction $\mathbf{\Omega}$ over the complete solid angle. The Discrete Ordinates Method is used to discretize $\mathbf{q}_\nu^{rad}$ into a set of 1-D steady state RTE. The integral over the solid angle is replaced by a weighted sum of discrete radiative intensities. Gaussian quadrature is employed to determine discrete directions $\mathbf{\Omega}_d$ and weights a_d for different degrees of approximation (N_d directions) as

$$\mathbf{q}_\nu^{rad} = \int_{4\pi} \mathbf{\Omega} \mathcal{I}_\nu(\mathbf{\Omega}) d\mathbf{\Omega} \approx \sum_{d=1}^{N_d} a_d \mathcal{I}_\nu^d \mathbf{\Omega}_d \tag{24}$$

For a non-scattering plasma, the 1-D steady state RTE of direction $\mathbf{\Omega}_d$ is expressed as

$$\mathbf{\Omega}_d \cdot \boldsymbol{\partial}_\mathbf{x} \mathcal{I}_\nu^d = \kappa_\nu B_\nu - \kappa_\nu \mathcal{I}_\nu^d \tag{25}$$

The linear absorption coefficient κ_ν was calculated following the Planck Mean Absorption Coefficient band-averaging model [9]. The Line-By-Line spectral properties in air plasma were computed by the Nonequilibrium Air Radiation (NEQAIR) program [45] using more than 500,000 wavelengths between 0.04 μm and 20 μm.

The banded black body spectral radiance intensity is given by

$$B_\nu(T) = \int_\nu^{\nu+1} \frac{2\mathcal{H}\nu^3}{c^2} \frac{1}{\exp(\mathcal{H}\nu/k_B T) - 1} d\nu \tag{26}$$

The left-hand side of Eq. (25) integrated over the cell volume gives

$$\int_{V_c} \mathbf{\Omega}_d \cdot \boldsymbol{\partial}_{\mathbf{x}} \mathcal{I}_\nu^d \, dV = \int_{V_c} \boldsymbol{\partial}_{\mathbf{x}} \cdot \left(\mathbf{\Omega}_d \mathcal{I}_\nu^d\right) dV = \int_{S_c} \mathcal{I}_\nu^d \, \mathbf{\Omega}_d \cdot \, d\mathbf{S} \approx \sum_{c=1}^{N_{nc}} \mathcal{I}_{\nu,c}^d \, \mathbf{\Omega}_d \cdot \mathbf{\Delta S_c} \tag{27}$$

The surface integral in Eq. (27) is approximated by a summation over the faces of face-centered values times the corresponding cell areas.

The right-hand side of Eq. (25) integrated over the cell volume gives

$$\int_{V_c} \kappa_\nu \left(B_\nu - \mathcal{I}_\nu^d\right) dV \approx \kappa_{\nu,c} \left(B_{\nu,c} - \mathcal{I}_{\nu,c}^d\right) V_c \tag{28}$$

The volume integral in Eq. (28) is approximated by the cell center value of the integrand times the cell volume. Eq. (27) and (28) give

$$\sum_{c=1}^{N_{nc}} \mathcal{I}_{\nu,c}^d \, \mathbf{\Omega}_d \cdot \mathbf{\Delta S_c} = \kappa_{\nu,c} \left(B_{\nu,c} - \mathcal{I}_{\nu,c}^d\right) V_c \tag{29}$$

As represented in Fig. 2, Eq. (29) is split into an incoming part ($k_i \in \mathbf{\Omega}_d \cdot \mathbf{\Delta S_c} < 0$) and an outgoing part ($k_o \in \mathbf{\Omega}_d \cdot \mathbf{\Delta S_c} > 0$). This is expressed in mathematical terms as

$$\sum_{k_i=1}^{N_{k_i}} \mathcal{I}_{\nu,k_i}^d \, \mathbf{\Omega}_d \cdot \mathbf{\Delta S_c} + \mathcal{I}_{\nu,c}^d \sum_{k_o=1}^{N_{k_o}} \mathbf{\Omega}_d \cdot \mathbf{\Delta S_c} = \kappa_{\nu,c} \left(B_{\nu,c} - \mathcal{I}_{\nu,c}^d\right) V_c. \tag{30}$$

Consequently, an explicit expression of the radiative intensity at the cell c is obtained as follows

$$\mathcal{I}_{\nu,c}^d = \frac{\sum_{k_i=1}^{N_{k_i}} \mathcal{I}_{\nu,k_i}^d \, \mathbf{\Omega}_d \cdot \mathbf{\Delta S_c} + \kappa_{\nu,c} B_{\nu,c} V_c}{\sum_{k_o=1}^{N_{k_o}} \mathbf{\Omega}_d \cdot \mathbf{\Delta S_c} + \kappa_{\nu,c} V_c} \tag{31}$$

$\mathcal{I}_{\nu,c}^d$ is solved in Eq. (31) for each band and direction following a specific order, different for each direction, represented in Fig. 2.

The divergence of the total radiative heat flux at each cell c is given by

$$\boldsymbol{\partial_x} \cdot \mathbf{q}_c^{rad} = \sum_{\nu=1}^{N_b} \sum_{d=1}^{N_d} \frac{a_d \mathcal{I}_{\nu,c}^d \boldsymbol{\Omega}_d \cdot \mathbf{\Delta S_c}}{V_c} \tag{32}$$

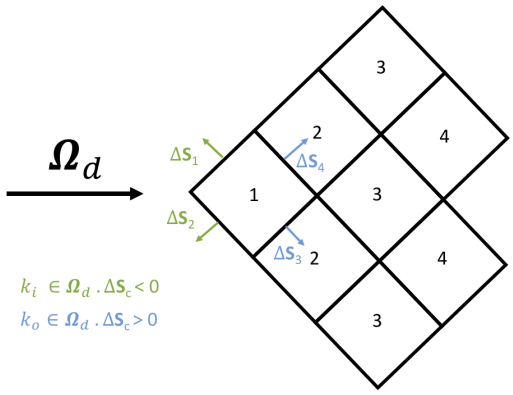

Figure 2: Representation of the directional split into an incoming and outgoing part and the specific advance order used in the computation of the radiative heat flux.

2.4. Boundary Conditions

The Boundary Conditions (BC) used are presented (see Fig. 3) in this section for the multiple physics phenomena involved in these arc heater simulations.

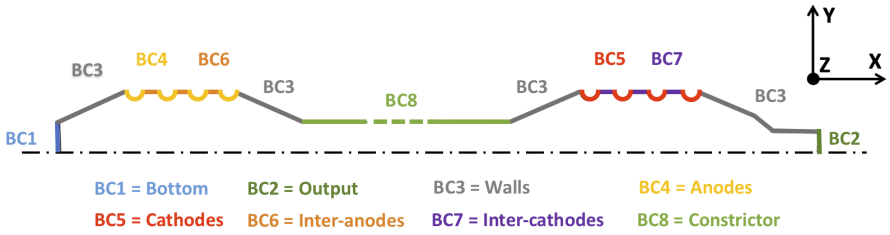

Figure 3: Representation of the boundary conditions in the studied arc heater. The flow is injected at the inter-anodes (BC6) and constrictor (BC8). BC2 is treated as an outflow boundary.

2.4.1. Flow

The water-cooled arc heater walls (BC3), constrictor (BC8), and inter-electrodes (BC6 and BC7) are assumed to be at a constant temperature. The electrodes (BC4 and BC5) and the outlet (BC2) are assumed adiabatic. A constant air inlet mass flux is imposed at the inter-anodes (BC6) and constrictor (BC8). The swirling inlet velocity is computed as follows

$$\boldsymbol{u} = \frac{-\dot{m}}{\rho\ |\boldsymbol{S}|}\ (\ \boldsymbol{n} + tan(\theta)\ \boldsymbol{t}\ ) \quad \text{with} \quad \boldsymbol{t} = \boldsymbol{n}_{axis} \times \boldsymbol{n}. \tag{33}$$

The tangential inclination angle is set at 45° to promote air mixing. Table 1 gives a summary of the BC that are used for the flow in this study.

	p [Pa]	**T [K]**	$\boldsymbol{u}$ **[m/s]**
$BC1$	$\boldsymbol{\partial_x} p \cdot \boldsymbol{n} = 0$	$T_w = 500$ K	$\boldsymbol{u} = \boldsymbol{0}$
$BC2$	$\boldsymbol{\partial_x} p \cdot \boldsymbol{n} = 0$	$\boldsymbol{\partial_x} T \cdot \boldsymbol{n} = 0$	$\boldsymbol{\partial_x u} \cdot \boldsymbol{n} = \boldsymbol{0}$
$BC3$	$\boldsymbol{\partial_x} p \cdot \boldsymbol{n} = 0$	$T_w = 500$ K	$\boldsymbol{u} = \boldsymbol{0}$
$BC4$	$\boldsymbol{\partial_x} p \cdot \boldsymbol{n} = 0$	$\boldsymbol{\partial_x} T \cdot \boldsymbol{n} = 0$	$\boldsymbol{u} = \boldsymbol{0}$
$BC5$	$\boldsymbol{\partial_x} p \cdot \boldsymbol{n} = 0$	$\boldsymbol{\partial_x} T \cdot \boldsymbol{n} = 0$	$\boldsymbol{u} = \boldsymbol{0}$
$BC6$	$\boldsymbol{\partial_x} p \cdot \boldsymbol{n} = 0$	$T_w = 500$ K	$\dot{m}_{BC6} = 0.05$ kg/s
$BC7$	$\boldsymbol{\partial_x} p \cdot \boldsymbol{n} = 0$	$T_w = 500$ K	$\boldsymbol{u} = \boldsymbol{0}$
$BC8$	$\boldsymbol{\partial_x} p \cdot \boldsymbol{n} = 0$	$T_w = 500$ K	$\dot{m}_{BC8} = 0.4$ kg/s

Table 1: Summary of the BC for the Navier-Stokes equations.

2.4.2. Electromagnetism

The power supply to the arc heater is a constant current supply, and therefore, the electric field will adjust to enable a constant current between the anode and cathode chambers. The anode current density is considered constant in this study, as follows

$$\sigma \boldsymbol{\partial_x} \phi_{imp,a_i} \cdot \mathbf{n} = -\mathbf{J}_{imp,a_i} \quad \text{and} \quad I_{imp,a_i} = \int_{S_{a_i}} \mathbf{J}_{imp,a_i} \cdot d\mathbf{S} \tag{34}$$

An unbalanced current at the electrodes will result in an uneven current attachment: the electrode with the highest current will experience the highest

heating near the surface, which results in the highest conductivity for the gas near the surface, thus reinforcing the location of this attachment. A stable concentrated current attachment will result in mechanical failure (erosion or melting) of the electrode. The use of a ballast configuration balances the electric potential at each electrode to force an even distribution of the total current. The same resistance is used for all electrodes. The configuration results in a mixed boundary condition at the cathodes. This reads in mathematical terms

$$-I_{imp,c_i} = \int_{S_{c_i}} \sigma \boldsymbol{\partial_x} \phi_{imp,c_i} \cdot \, d\mathbf{S} = \frac{1}{R_b}(\phi_{imp,c_i} - \phi_G) \tag{35}$$

An explicit scheme is used to impose the above BC. This is done by setting the potential at the discretized time step n to

$$\phi^n_{imp,c_i} = \phi_G - R_b I^{n-1}_{imp,c_i} \tag{36}$$

with $I^0_{imp,c_i} = 0$ initially, otherwise

$$I^{n-1}_{imp,c_i} = \int_{S_{c_i}} -\sigma \boldsymbol{\partial_x} \phi^{n-1}_{imp,c_i} \cdot \, d\mathbf{S} \tag{37}$$

i.e., the potential at the cathodes is adjusted by using the electric current from the previous time step. Note that the continuity of the electric current ensures that

$$-\sum_{i=1}^{N_{c_i}} I_{imp,c_i} = \sum_{i=1}^{N_{a_i}} I_{imp,a_i} = I_{imp,tot} \tag{38}$$

The walls of segmented arc heaters are water-cooled copper rings that are isolated from each other by thin ceramic (non-conductive) spacers. The rings are electrically isolated from the ground, and the spacers prevent current along the walls. In this configuration, electrically floating rings ensure proper adjustment of the electric potential. The walls of the constrictor are made of floating rings except at the electrodes where voltage is applied to ensure constant current. As

such, charge will accumulate in each ring so that

$$\boldsymbol{J}_{imp,w} = \mathbf{0} \tag{39}$$

Thus, the electrical potential boundary condition at the wall is

$$\boldsymbol{\partial_x}\phi_{imp,w} \cdot \mathbf{n} = 0 \tag{40}$$

Table 2 summarizes the BC that are used for the electromagnetic equations in this simulation.

	ϕ_{imp} [V]	$\boldsymbol{A}_{imp}$ [T · m]	$\boldsymbol{A}_e$ [T · m]
$BC1$	$\boldsymbol{\partial_x}\phi_{imp} \cdot \boldsymbol{n} = 0$	$\boldsymbol{A}_{imp} = \mathbf{0}$	$\boldsymbol{A}_e = \mathbf{0}$
$BC2$	$\boldsymbol{\partial_x}\phi_{imp} \cdot \boldsymbol{n} = 0$	$\boldsymbol{A}_{imp} = \mathbf{0}$	$\boldsymbol{A}_e = \mathbf{0}$
$BC3$	$\boldsymbol{\partial_x}\phi_{imp} \cdot \boldsymbol{n} = 0$	$\boldsymbol{A}_{imp} = \mathbf{0}$	$\boldsymbol{A}_e = \mathbf{0}$
$BC4$	$I_{imp,tot} = 1200$ A	$\boldsymbol{A}_{imp} = \mathbf{0}$	$\boldsymbol{A}_e = \mathbf{0}$
$BC5$	$\phi^n_{imp,c_i} = \phi_G - R_b I^{n-1}_{imp,c_i}$	$\boldsymbol{A}_{imp} = \mathbf{0}$	$\boldsymbol{A}_e = \mathbf{0}$
$BC6$	$\boldsymbol{\partial_x}\phi_{imp} \cdot \boldsymbol{n} = 0$	$\boldsymbol{A}_{imp} = \mathbf{0}$	$\boldsymbol{A}_e = \mathbf{0}$
$BC7$	$\boldsymbol{\partial_x}\phi_{imp} \cdot \boldsymbol{n} = 0$	$\boldsymbol{A}_{imp} = \mathbf{0}$	$\boldsymbol{A}_e = \mathbf{0}$
$BC8$	$\boldsymbol{\partial_x}\phi_{imp} \cdot \boldsymbol{n} = 0$	$\boldsymbol{A}_{imp} = \mathbf{0}$	$\boldsymbol{A}_e = \mathbf{0}$

Table 2: Summary of the BC for the Maxwell equations.

2.4.3. Radiation

The walls are made of unpolished copper and are assumed to behave as a gray body at the wall temperature. We set the emissivity of copper $\epsilon_\nu = 0.6$, constant for all wavelengths. The average radiative intensity from the wall surface, emitted by each band, is given by

$$\mathcal{I}^d_{\nu,w} = \epsilon_\nu B_\nu \tag{41}$$

3. Numerical model

The numerical framework is based on OpenFOAM, an open-source, modern, and modular C++ finite volume library. This framework offers a wide range of numerical schemes, interpolation schemes, integration methods, turbulence models, thermodynamic models, and flow solvers. The governing equations are sequentially solved as explained in Algorithm 1. The OpenFOAM semi-discrete finite volume solver rhoCentralFoam has been chosen for modeling the flow. The non-staggered central scheme that is used in this solver has proven to be accurate in the simulations of high-speed compressible flows [13]. Additionally, a $k - \epsilon$ model is applied to the flow turbulence [7]. Second order accuracy in space is achieved with a total variation diminishing (TVD) scheme with van Albada's limiter [41]. The Maxwell equations, described in Eq. (13) and (16), that link the electric and magnetic fields are computed by using a generalized Geometric-Algebraic Multi-Grid (GAMG) solver. The Mutation++ library [35], dynamically linked to the OpenFOAM thermodynamic framework, is used to compute equilibrium chemistry compositions and thermodynamic and transport properties, as detailed in Appendix A. The discretization of radiative heat flux uses a multi-band approximation of the non-gray spectral properties of high-temperature air. The radiative directional integration is determined by a Gaussian type quadrature. The contributions of the electric field, magnetic field, and radiative heat flux are added as source terms to the momentum and energy equations.

Algorithm 1 ARCHeS

function MAIN
  create time and mesh
  read and initialize user configurations
    ▷ flags for radiation and electromagnetism
  read fields p^0, T^0, $\boldsymbol{u}^0$, ϕ^0, $\boldsymbol{A}^0$, $\boldsymbol{\partial_x} \cdot \boldsymbol{q}^0_{rad}$
  compute α^0, ψ^0, μ^0, σ^0, γ^0, e^0, ρ^0
    ▷ thermodynamics in function of p^0, T^0
  initialize radiation and electromagnetism
  while RunTime **do**
    correct boundary conditions for $\boldsymbol{u}^n$, σ^n, ϕ^n
    compute ϕ^{n+1}, $\boldsymbol{A}^{n+1}$
      ▷ solve electromagnetic equations
    compute $\boldsymbol{\partial_x} \cdot \boldsymbol{q}^{n+1}_{rad}$
      ▷ solve radiation
    compute fluxes and source terms
    compute ρ^{n+1}
      ▷ solve mass equation
    compute $\boldsymbol{u}^{n+1}$
      ▷ solve momentum equations
    compute e^{n+1}
      ▷ solve energy equation
    compute T^{n+1}
    compute α^{n+1}, ψ^{n+1}, μ^{n+1}, σ^{n+1}, γ^{n+1}
      ▷ thermodynamics in function of p^n, T^{n+1}
    compute p^{n+1}
    correct p^{n+1}, ρ^{n+1} boundaries
    compute μ^{n+1}_{eff}, and α^{n+1}_{eff}
      ▷ solve $k - \epsilon$ turbulence equations
    write fields

4. Results

4.1. Flow

Figure 4 shows the pressure and temperature profiles along the centerline axis of the arc heater. The pressure has a maximum value of 13.3 atm, almost steady in the anode chamber. The pressure gently decreases along the constrictor from 13.2 to 9.2 atm. The pressure stays constant in the cathode chamber and then drops again in the convergent part. The pressure is about 3.5 atm at the nozzle throat. The time-averaged temperature computed from 0.4640 s to 0.5759 s has a maximum value of ∼8000 K. The temperature increases in the anode chamber. The instantaneous time values of the temperature highly fluctuate in the constructor as a consequence of the arc instabilities. The temperature drops from 7500 K at the cathode chamber to 4400 K at the nozzle throat.

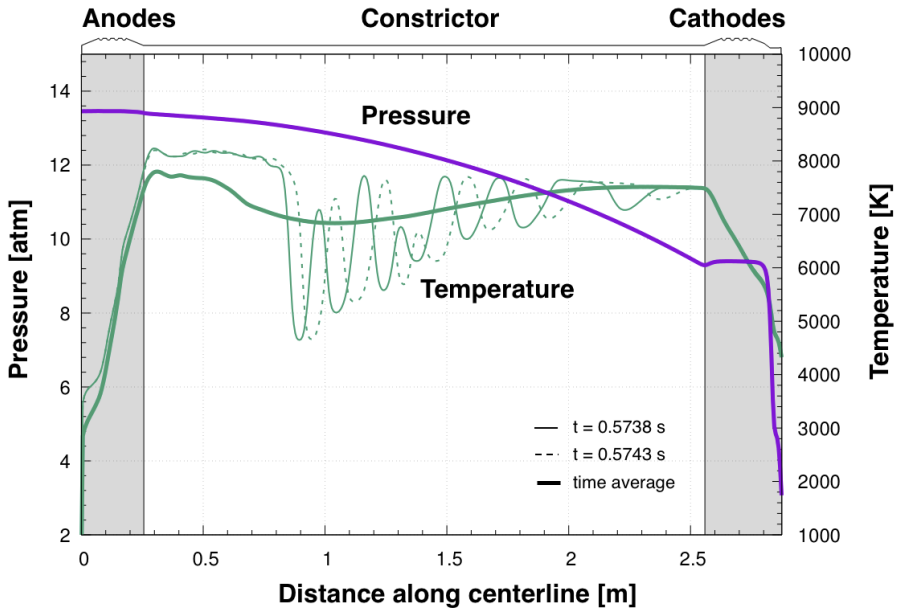

Figure 4: Pressure and temperature profiles along the centerline axis.

Figure 5 shows the enthalpy and velocity profiles along the centerline axis of the arc heater. The time-averaged enthalpy and velocity were computed from 0.4640 s to 0.5759 s. The enthalpy follows the trend of the temperature (Fig.

4). The maximum of the time-averaged enthalpy is about 24 MJ $\cdot$ kg^{-1}. For both instantaneous and time-averaged, the gas enthalpy increases in the anode chamber and decreases in the cathode chamber. In the constrictor region, the averaged value drops only to increase again so that the value at the exit of the constrictor is similar to the one at the entrance. Alternatively, instantaneous values show high fluctuation that is indicative of arc instabilities. Instantaneous and time-averaged velocities along the centerline follow a similar trend. The velocity is low in the anode chamber due to the absence of air injection, which is introduced along the inter-anodes and the constrictor (Fig. 3). The velocity increases up to 550 m $\cdot$ s^{-1} in the constrictor, drops in the divergent part, and increases again in the convergent part of the cathode chamber. The flow is subsonic in the anode chamber, the constrictor, and the cathode chamber. The Mach number equals 1 at the nozzle throat. The flow becomes supersonic after the nozzle throat.

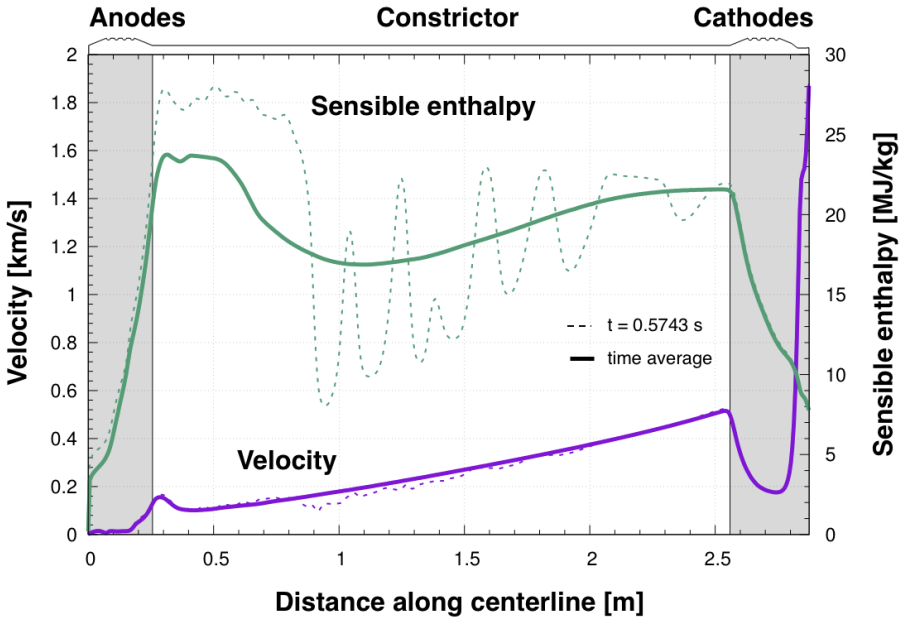

Figure 5: Velocity and enthalpy profiles along the centerline axis.

Figure 6 shows the XY cutting plane of the temperature from the anode

chamber to the nozzle throat. The highest temperature (around 8000 K) is close to the centerline axis because of the low temperature imposed at the water-cooled walls. Arc instabilities are visible in the constrictor. A three-dimensional unsteady modeling tool is needed to capture these instabilities.

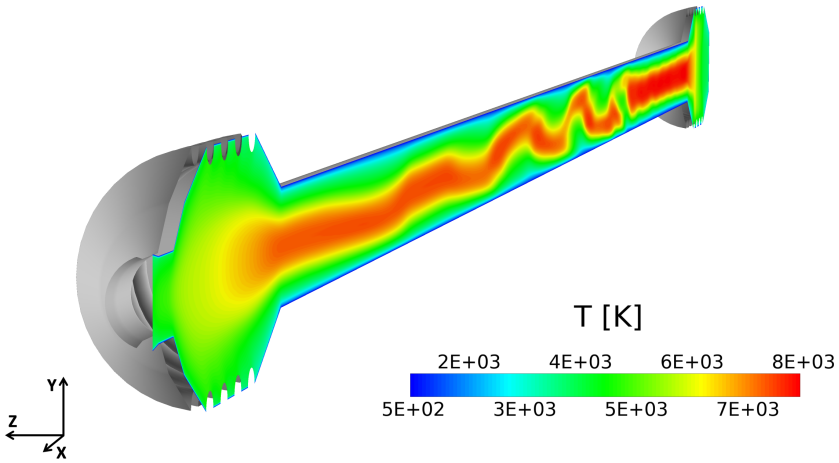

Figure 6: Temperature XY cutting plane from the anode chamber to the nozzle throat, t = 0.5738 s.

Figure 7 shows the YZ cutting plane of the temperature for different times at X = 1.5 m. The shape of the high-temperature electric arc core shows an unsteady behavior. The dynamic of the arc indicates that the instability saturates next to the wall. The core cannot get close to the constrictor wall due to the injection of low-temperature air and due to the water cooling system.

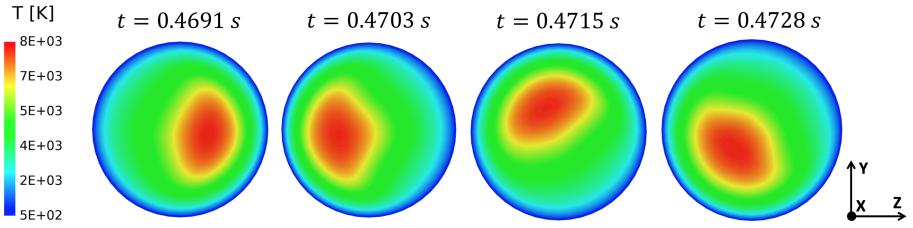

Figure 7: Temperature YZ cutting plane at X = 1.5 m for different times.

Figures 8 and 9 show the XY cutting plane of the velocity at the cathode

and anode chambers. The inlet mass flow is 0.05 kg $\cdot$ s^{-1} in the anode chamber and 0.4 kg $\cdot$ s^{-1} in the constrictor. The gas velocity is higher next to the centerline axis. The highest velocity of 1.9 km $\cdot$ s^{-1} is located at the end of the computational domain, just after the nozzle throat. Figure 9 shows that the flow is impacted by the arc instabilities in the constrictor.

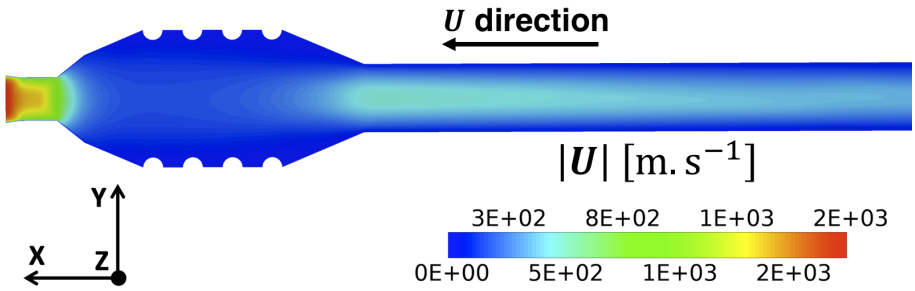

Figure 8: Velocity XY cutting plane in the constrictor and the cathode chamber, t = 0.5738 s.

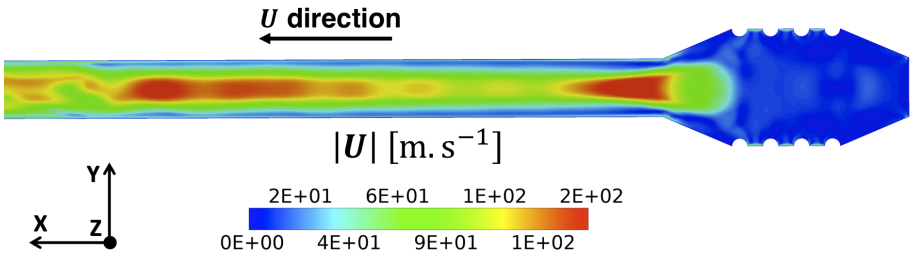

Figure 9: Velocity XY cutting plane in the constrictor and the anode chamber, t = 0.5738 s.

Figure 10 shows cutting planes of the vorticity $\boldsymbol{\omega}$ computed as follows

$$\boldsymbol{\omega} = \boldsymbol{\partial_x} \times \boldsymbol{u} \tag{42}$$

As described in section 2.4, the flow is injected at the inter-anodes and constrictor. The XY cutting plane shows the vorticity magnitude for the entire geometry. The highest vorticity magnitude is located close to the wall. The YZ cutting planes show the vorticity magnitude in color, the YZ velocity $\boldsymbol{u}_{yz}$ using streamlines at X = [1, 1.5] m, and the axial velocity $\boldsymbol{u}_x$ at X = 2 m. The

locations of the vortex cores change along the centerline axis, and the velocity is mainly axial at X = 2 m. Future work will study the strong interactions between wall shear and arc instabilities that impact the vorticity and play an essential role in flow mixing.

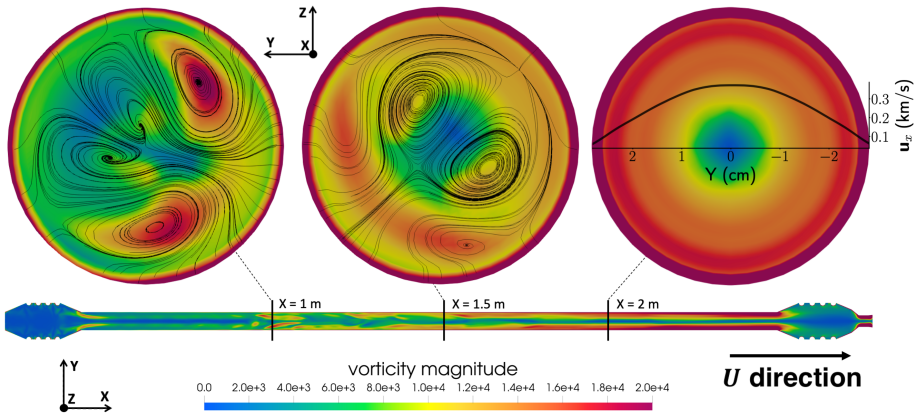

Figure 10: XY and YZ cutting planes of the vorticity $\boldsymbol{\omega}$, t = 0.5738 s. The color shows the vorticity magnitude, the streamlines represent the velocity in the YZ plane $\boldsymbol{u}_{yz}$ at X = [1, 1.5] m, and the plot shows the axial velocity $\boldsymbol{u}_x$ at X = 2 m.

4.2. Electromagnetism and radiation

Figure 11 shows the comparison between the Joule heating and radiative heating/cooling profiles along the centerline axis. The radiative heat flux is the predominant cooling process of the gas medium. In the same figure, a snapshot of the radiative heating/cooling and Joule heating profiles presents fluctuations along the axis resulting from the electric arc instabilities. The radiative heating/cooling follows the Joule heating curve trend and is mostly negligible along the constrictor centerline. Joule heating is almost null at the start of the anode chamber and at the end of the cathode chamber.

Figure 12 shows the Joule heating and the radiative heating/cooling profiles along the radial axis at half-length of the constrictor. The radiative cooling ($\boldsymbol{\partial_x} \cdot \boldsymbol{q^{rad}} > 0$) is due to the re-radiation of the heat from the electric arc core, where the temperature is the highest. The radiative cooling is almost negligible compared to Joule heating. The radiative heating ($\boldsymbol{\partial_x} \cdot \boldsymbol{q^{rad}} < 0$) is strong

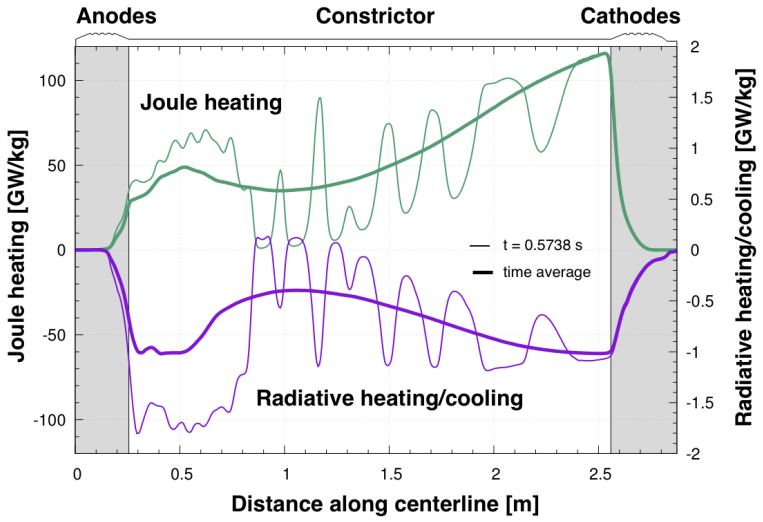

Figure 11: Joule heating ($|\boldsymbol{J}_{imp}|$) and radiative heating/cooling ($-\boldsymbol{\partial_x} \cdot \boldsymbol{q^{rad}}$) profiles along the centerline axis.

outside the electric arc core and is higher than the Joule heating next to the wall (2.30 cm $<$ radius $<$ 2.85 cm).

Figure 13 shows the cutting plane of the radiative heating/cooling from the anode chamber to the nozzle throat. The blue color represents the radiative cooling ($\boldsymbol{\partial_x} \cdot \boldsymbol{q^{rad}} > 0$) which occurs at the center of the electric arc. The red color shows the radiative heating ($\boldsymbol{\partial_x} \cdot \boldsymbol{q^{rad}} < 0$) at the surroundings of the electric arc core. The transverse cutting planes show the electric arc instabilities and the importance of the three-dimensional calculations of the radiation. In this work, the discretization of the radiative heat flux is done using 24 discrete directions and 100 spectral bands.

Figure 14 shows the cutting plane of the imposed current density from the anode chamber to the nozzle throat. The current density is mainly constrained close to the centerline of the constrictor due to the cold injection of air at the wall. The total current is equally distributed among the anodes due to the BC explained in Eq. (34). The continuity of current from Eq. (13) imposes the same total current at the anodes and the cathodes. The electric ballast system,

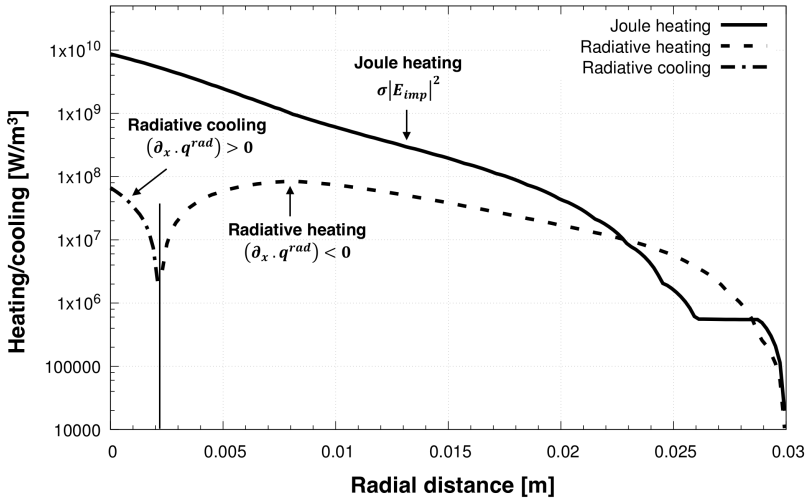

Figure 12: Joule heating and radiative heating/cooling profile in the radial direction halfway along the constrictor, t = 0.5738 s.

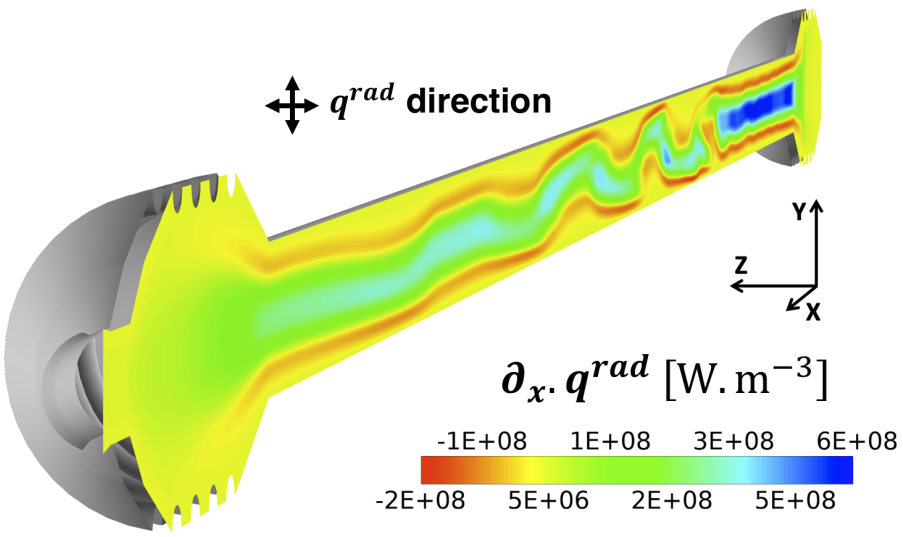

Figure 13: Divergence of the radiative heat flux from the anode chamber to the nozzle throat, t = 0.5738 s. The blue and red colors correspond to radiative cooling and heating, respectively.

implemented using Eq. (37), balances the current at each cathode to force an even distribution. The peak of the imposed current density is about 3 MA · m^{-2}.

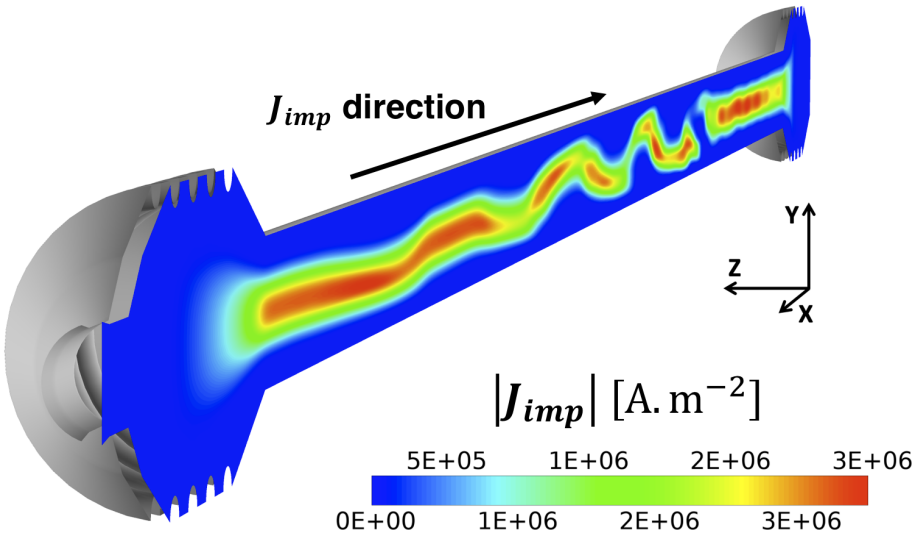

Figure 14: Imposed current density from the anode chamber to the nozzle throat, t = 0.5738 s.

Figure 15 shows the cutting plane of the imposed magnetic field from the anode chamber to the nozzle throat. The imposed magnetic field is generated around the imposed current density according to Ampere's law (Eq. (3)). The maximum magnitude of the imposed magnetic field is about 0.02 T. The magnetic field direction is mainly perpendicular to the imposed current density. The magnetic field is null at the center of the electric arc and increases in the radial direction. Towards the wall, it decreases again. The curvature of the electric arc creates a stronger magnetic field at the concave part of the electric arc, which results in the kink instability that is shown in Fig. 15. The intensity of the imposed magnetic field decreases in the electrode chambers due to the more diffuse imposed current density.

Figure 16 shows the cutting plane of the external magnetic field created by the electrodes from the anode chamber to the nozzle throat. The magnitude

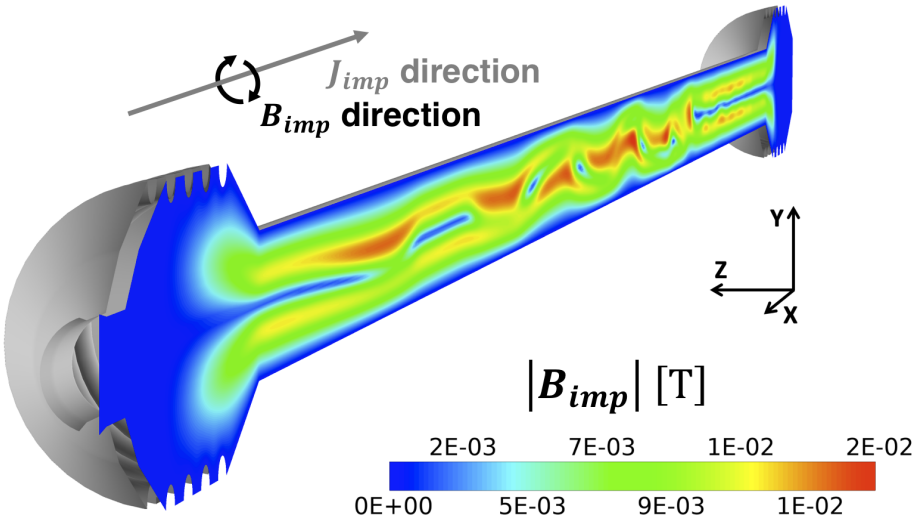

Figure 15: Imposed magnetic field from the anode chamber to the nozzle throat, t = 0.5738 s.

of the external magnetic field is almost null in the constrictor. The maximum magnitude is about 0.01 T and is found around the electrodes. The direction is primarily longitudinal to the imposed current density direction.

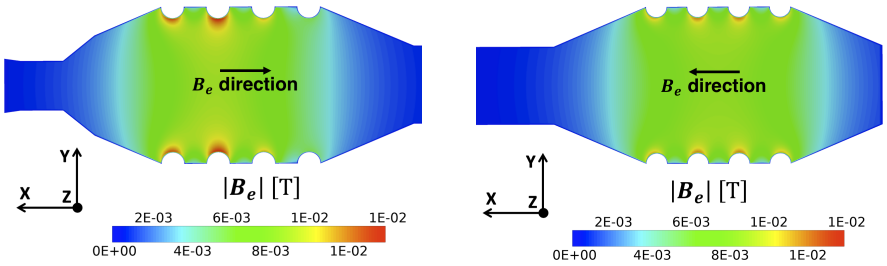

Figure 16: External magnetic field in the cathode (left) and anode (right) chambers, t = 0.5738 s.

Figure 17 shows the current as a function of time at the different cathodes. The sum of the 4 cathode currents gives a total current of 1170 A. Cathode 1 is the closest electrode to the constrictor. Cathode 4 is the nearest electrode to the nozzle throat. A peak of current appears on all the electrodes at 0.487 s. Then the 4 currents stabilize to a quasi constant value. The simulation seems

to achieve a statistically steady state.

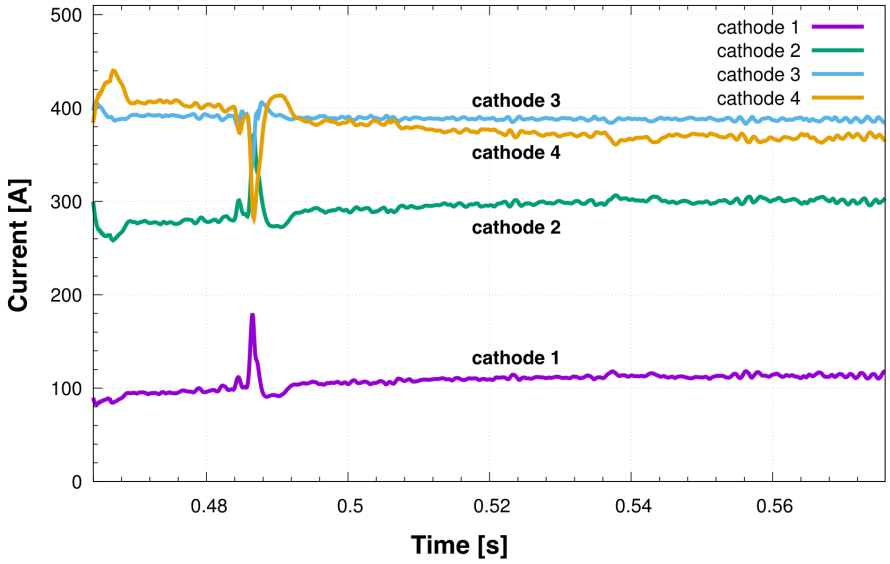

Figure 17: Current at the cathodes as a function of time.

4.3. Arc instabilities

Trelles [38] describes different types of instabilities that can play a dominant role in the dynamic geometry of a constrained electric arc. The fluid dynamic instabilities are produced by the large gradient of velocity, temperature, density, and viscosity between the cold gas and the plasma created by Joule heating. Shear flow instabilities are often considered one of the most prominent, leading to the growth of a small perturbation downstream that may drive the flow from laminar to turbulent. The thermal instabilities are caused by the non-uniform cooling of the plasma that produces a deflection of the electric arc. The injection of cold gas forces the arc to deviate away from the cold source. The magnetic field, both the external and that self-induced by the electric current, is responsible for the sausage and kink instabilities. The non-uniform plasma distribution and the curvature of the magnetic field impact these instabilities. Sausage instabilities occur when there is a change of cross section in the electric

arc. In this regard, a smaller cross section translates to a stronger magnetic field. Kink instabilities occur when the electric arc curves. Figure 18 shows the iso-surface of the imposed current density at 1 MA $\cdot$ m^{-2}, a value representative of the main part of the electric arc. The color represents the magnitude of the total magnetic field. For high current density, the total magnetic field is primarily due to the imposed magnetic field in the constrictor. Even though the arc instabilities in Fig. 18 are a combination of all the instabilities, the kink instability is visible where the magnetic field is stronger on the concave side and weaker on the convex side of the plasma column. The electric arc seems to stabilize at the entrance of the electrode chambers. More advanced analysis of the arc behavior is required to fully understand and characterize the complex dynamic interaction of the cold gas as well as the inherent properties of thermal plasma. Future work will see the implementation of finite-rate chemistry in the existing model and may lead to new insights in low-pressure regions where the assumption of Local Thermal Equilibrium (LTE) breaks down.

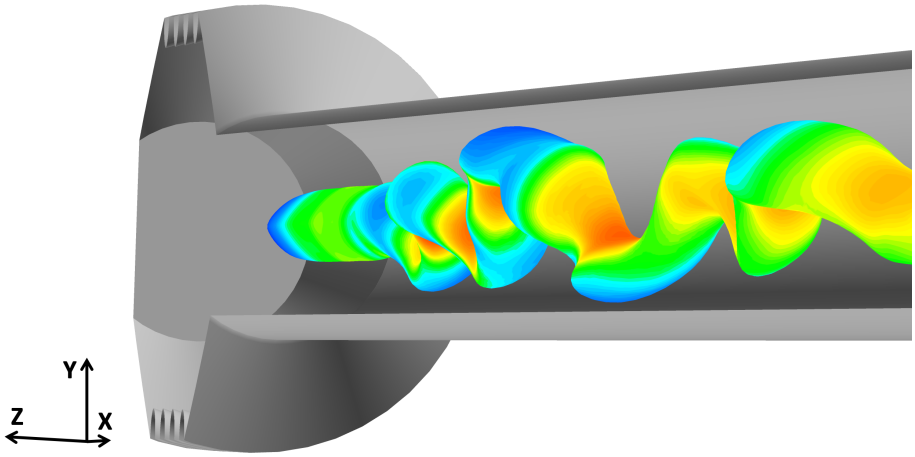

Figure 18: Arc instabilities in the constrictor, t = 0.5738 s. The iso-surface shows the current density (1 MA $\cdot$ m^{-2}). The color represents the magnitude of the total magnetic field.

4.4. Arc attachment

Figures 19 and 20 show the iso-surface of the current density (30 kA $\cdot$ m^{-2}) at two different times (t = 0.4785 s and t = 0.4880 s). The color represents the magnitude of the total magnetic field. The external magnetic field, predominantly present around the electrode chambers, has a more significant influence on the arc attachment to the electrodes than the imposed magnetic field, almost negligible in these regions. The Neumann boundary condition of the imposed electric potential forces a constant and uniform current density among the anodes. On the other hand, the Dirichlet boundary condition at the cathodes sets a constant imposed electric potential, which translates to a non-uniform and non-constant electric current among the cathodes. The location of the arc attachment changes over time at the cathodes. The high temperature in the cathode chamber makes the air conductive and allows a diffuse arc attachment. The ballast configuration balances the electric potential at each electrode to force an even distribution of the total current. It is shown that the attachment at the cathodes is mainly driven by the upstream arc instabilities. The kink instabilities generated in the constrictor force the arc to move closer to a specific region of the electrodes, which, in turn, provokes the attachment of the arc. Unlike the studies from Trelles [38], this LTE model does not need an artificially high electric conductivity near the cathodes by choosing an interpolation scheme that conserves the electric flux.

5. Conclusion

Further development of arc jet technologies has been limited by an incomplete understanding of unstable plasma flow occurring in the constricted arc heater. The direct observation of the complete arc dynamics is extremely difficult inside an arc jet, and its numerical modeling is highly challenging. The complexity of plasma flow simulations comes from the partial knowledge of constrained arc instabilities. The interactions of cold gas and plasma flow are strongly influenced by the radiation and the magnetic field that lead to com-

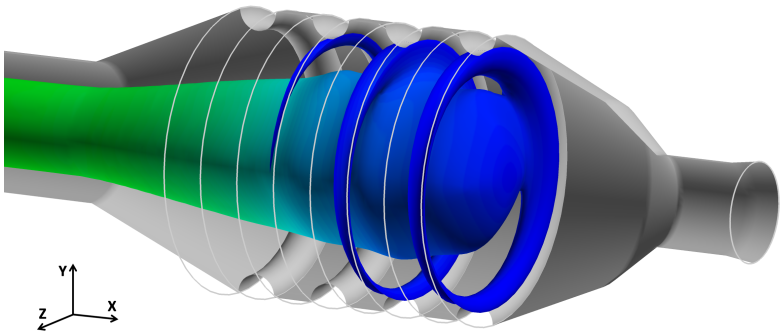

Figure 19: Arc attachment at the cathodes, t = 0.4785 s. The iso-surface shows the current density (30 kA $\cdot$ m^{-2}). The color represents the magnitude of the total magnetic field.

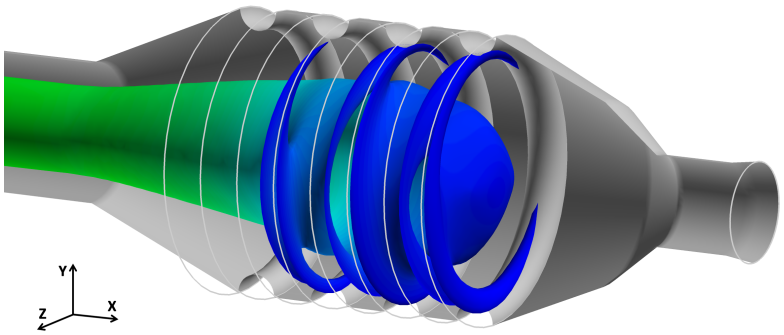

Figure 20: Arc attachment at the cathodes, t = 0.4880 s. The iso-surface shows the current density (30 kA $\cdot$ m^{-2}). The color represents the magnitude of the total magnetic field.

plicated coupled instabilities. A separation of the different physics involved is necessary to understand these instabilities. Arc attachment at the electrodes is a central part of the dynamics of the arc. The development of the analysis tool ARC Heater Simulator (ARCHeS) software provides the capability to perform three-dimensional time-dependent plasma flow simulations, which are necessary to capture the complex behavior of the arc. The massively parallel simulation support inherited in ARCHeS from its modular OpenFOAM architecture makes this work possible. This tool provides estimates of the flow state at the inlet of the nozzle, which are used as inlet conditions for well-established aerothermal techniques for estimating the aerothermal environment at the test articles. The formulation used in ARCHeS has been demonstrated to be efficient to attain convergence on very stiff non-linear systems encountered in plasma flow simulations. The unsteady flow is simulated from the anode chamber to the nozzle throat. Local Thermodynamic Equilibrium is assumed in the high-pressure arc heater. The imposed electric potential, the imposed magnetic field, and the external magnetic field are computed through Maxwell equations using a generalized geometric-algebraic multi-grid solver and are coupled to the flow through the Navier-Stokes equations. The three-dimensional radiation is solved using an accurate multi-band spectral discretization and Gaussian quadrature directional discretization. The inlet mass flux and the total current were chosen to be close to the operating conditions of large arc jet complexes used for TPS evaluation. These numerical simulations performed on NASA's Pleiades supercomputer have demonstrated their suitability for describing electric arc/cold flow interactions and flow instabilities encountered in arc heaters. This model is capable of describing the arc behavior and attachment at the cathodes without adding a reattachment model. The magnetic field plays an essential role in the flow characterization from the anode chamber to the nozzle throat. The location and frequency of the arc attachment at the cathodes are mainly driven by the upstream arc instabilities. A more complex analysis of the instabilities is needed to explain certain arc behaviors, such as the stabilization at the electrode chambers. The high computational cost of these simulations limits

the spatial resolution for wall turbulence analysis. These numerical simulations were obtained using 1200 cores of the NASA's Pleiades supercomputer during three weeks, i.e., approximately 6×10^5 core-hours. Comparison to measurements within arc heaters, such as those of Winter et al. [47], is still needed to validate this study. These experimental data are difficult to obtain due to the extremely harsh environment within the heaters. Future work should include a non-adiabatic boundary condition of the temperature at the electrodes. This requires a two-temperature model as well as a model of the energy transfer between the electrodes and the gas. The assumption of equilibrium chemistry in the entire arc heater from the anode chamber to the nozzle throat must be verified by adding a finite-rate chemistry model coupled with the fluid. Including heavy species in the thermodynamic and transport properties in addition to this model may pave the way to new areas of research, including the simulations of other complex plasma applications such as space propulsion. Even though large research efforts are still needed, this work has proven the effectiveness and efficiency of a finite volume approach for obtaining high-fidelity modeling of the governing equations involved in thermal plasma flows.

6. Acknowledgments

This work was supported by the Entry Systems Modeling project (Michael Barnhardt project manager and Aaron Brandis principal investigator) as part of the NASA Game Changing Development program. Authors Jeremie B. E. Meurisse and Nagi N. Mansour were funded by NASA contract NNA15BB15C to Analytical Mechanics Associates (AMA), Inc. The authors would like to acknowledge Alan A. Wray (NASA Ames Research Center), Sander J. Visser (AMA, Inc.), Sergio Fraile Izquierdo (AMA, Inc.), Federico Semeraro (AMA, Inc.), Joseph C. Schulz (AMA, Inc.), Magnus Haw (AMA, Inc.), and Francesco Panerai (University of Illinois at Urbana-Champaign) for their review of this document and their useful discussions.

Appendix A. Thermodynamic and transport properties

The equilibrium chemistry compositions and the thermodynamic and transport properties (Fig. A.21, A.22, and A.23) are computed using the Mutation++ library [35]. LTE is assumed in the entire domain. Most of the domain where the arc instabilities occur has a high pressure (Fig. 4) which justifies the use of LTE. Future work will take into account the low-pressure regions where LTE breaks down. The air mixture used in this work is composed of the following 13 species: e^-, N, N^+, O, O^+. NO, NO^+, N_2, N_2^+, O_2, O_2^+, Ar and Ar^+.

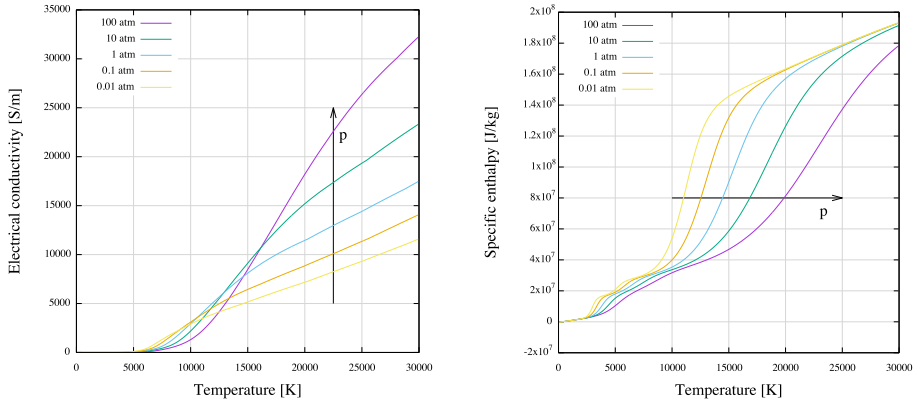

Figure A.21: Electrical conductivity (left) and enthalpy (right) as a function of temperature.

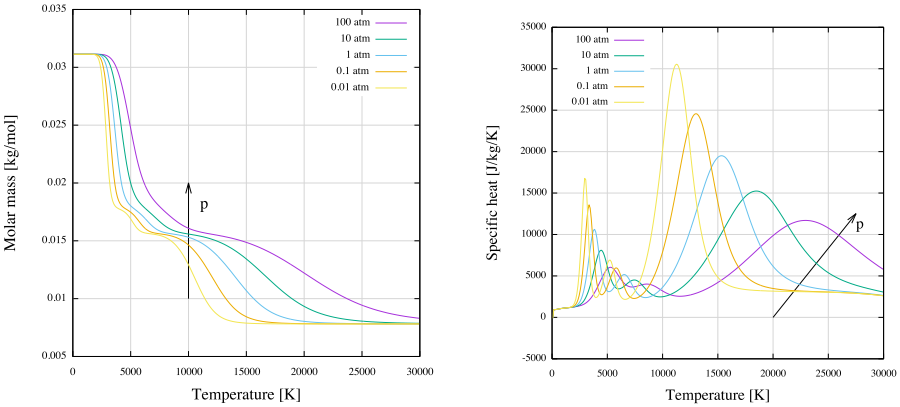

Figure A.22: Molar mass (left) and specific heat (right) as a function of temperature.

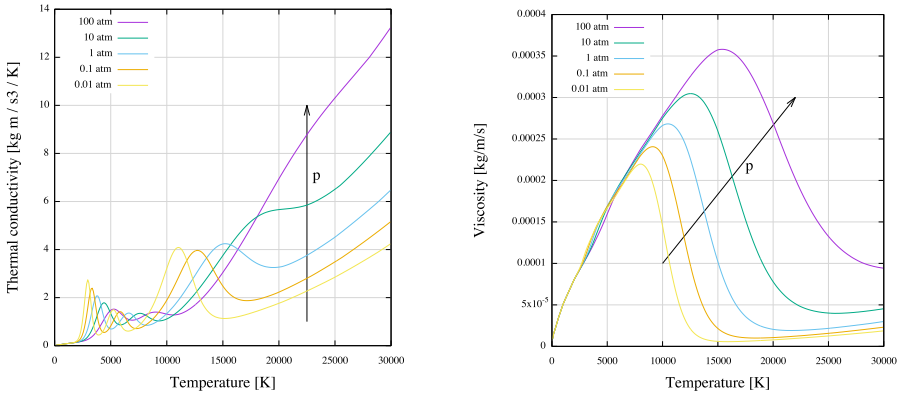

Figure A.23: Thermal conductivity (left) and viscosity (right) as a function of temperature.

References

[1] K.-i. Abe, T. Kameyama, H. Kihara, M. Nishida, K. Ito, and H. Tanno. Computation and experiment of nonequilibrium nozzle flow of arc-heated air. *Journal of thermophysics and heat transfer*, 19(4):428–434, 2005.

[2] M. A. Birkan. Arcjets and arc heaters-An overview of research status and needs. *Journal of Propulsion and Power*, 12(6):1011–1017, 1996.

[3] A. Borner, F. Panerai, and N. N. Mansour. High temperature permeability of fibrous materials using direct simulation Monte Carlo. *International Journal of Heat and Mass Transfer*, 106:1318 – 1326, 2017.

[4] P. Coelho. Bounded skew high-order resolution schemes for the discrete ordinates method. *Journal of Computational physics*, 175(2):412–437, 2002.

[5] J. F. Coudert and P. Fauchais. Transient Phenomena in dc Plasma-Spray Torches. *Annals of the New York Academy of Sciences*, 891(1):382–390, 1999.

[6] K. T. Edquist, B. R. Hollis, C. O. Johnston, D. Bose, T. R. White, and M. Mahzari. Mars Science Laboratory Heatshield Aerothermodynamics: Design and Reconstruction. *Journal of Spacecraft and Rockets*, 2014.

[7] S. El Tahry. k-epsilon equation for compressible reciprocating engine flows. *Journal of Energy*, 7(4):345–353, 1983.

[8] J. C. Ferguson, F. Panerai, J. Lachaud, and N. N. Mansour. Theoretical study on the micro-scale oxidation of resin-infused carbon ablators. *Carbon*, 121:552–562, 2017.

[9] S. Fraile Izquierdo, J. B. Meurisse, S. J. Visser, M. A. Haw, J. Schulz, and N. Mansour. Analysis of Three Multi-Band Models for Radiative Heat Transfer in LTE Air Plasma. In *AIAA Scitech 2020 Forum*, page 0735, 2020.

[10] D. Giordano. Hypersonic-flow governing equations with electromagnetic fields. In *33rd Plasmadynamics and Lasers Conference*, page 2165, 2002.

[11] A. N. Gleizes, J. J. Gonzalez, B. Liani, and G. Raynal. Calculation of net emission coefficient of thermal plasmas in mixtures of gas with metallic vapour. *Journal of Physics D*, 26:1921–1927, 1993.

[12] J. Goedbloed and S. Poedts. *Principles of Magnetohydrodynamics: With Applications to Laboratory and Astrophysical Plasmas*. Cambridge University Press, 2004.

[13] C. J. Greenshields, H. G. Weller, L. Gasparini, and J. M. Reese. Implementation of semi-discrete, non-staggered central schemes in a colocated, polyhedral, finite volume framework, for high-speed viscous flows. *International journal for numerical methods in fluids*, 63(1):1–21, 2010.

[14] D. J. Griffiths. *Introduction to electrodynamics*. Prentice Hall, 1962.

[15] J. Grinstead, D. Stewart, and C. Smith. High enthalpy test methodologies for thermal protection systems development at NASA Ames research center. In *AIAA/CIRA 13th International Space Planes and Hypersonics Systems and Technologies Conference*, page 3326, 2005.

[16] B. S. Kirk and G. F. Carey. Development and validation of a SUPG finite element scheme for the compressible Navier–Stokes equations using a modified inviscid flux discretization. *International journal for numerical methods in fluids*, 57(3):265–293, 2008.

[17] B. S. Kirk, R. H. Stogner, T. A. Oliver, and P. T. Bauman. Recent advancements in fully implicit numerical methods for hypersonic reacting flows. *AIAA Paper*, 2559, 2013.

[18] J.-I. Lee, S.-H. Han, C. Kim, and K.-H. Kim. Analysis of Segmented Arc-Heater Flows with High Argon Concentration. *Journal of thermophysics and heat transfer*, 22(2):187–200, 2008.

[19] J.-I. Lee, C. Kim, and K.-H. Kim. Accurate computations of arc-heater flows using two-equation turbulence models. *Journal of thermophysics and heat transfer*, 21(1):67–76, 2007.

[20] L. Liu and H. Tan. Transient temperature response in semitransparent variable refractive index medium subjected to a pulse irradiation. *Journal of Quantitative Spectroscopy and Radiative Transfer*, 83(3):333–344, 2004.

[21] J. Lowke and E. Capriotti. Calculation of temperature profiles of high pressure electric arcs using the diffusion approximation for radiation transfer. *Journal of Quantitative Spectroscopy and Radiative Transfer*, 9(2):207–236, 1969.

[22] R. G. McClarren and C. D. Hauck. Robust and accurate filtered spherical harmonics expansions for radiative transfer. *Journal of Computational Physics*, 229(16):5597–5614, 2010.

[23] J. B. E. Meurisse, J. Lachaud, F. Panerai, C. Tang, and N. N. Mansour. Multidimensional material response simulations of a full-scale tiled ablative heatshield. *Aerospace Science and Technology*, 2018.

[24] M. F. Modest. Narrow-band and full-spectrum k-distributions for radiative heat transfer-correlated-k vs. scaling approximation. *Journal of Quantitative Spectroscopy and Radiative Transfer*, 76(1):69–83, 2003.

[25] J. Murthy and S. Mathur. Finite volume method for radiative heat transfer using unstructured meshes. *Journal of thermophysics and heat transfer*, 12(3):313–321, 1998.

[26] F. Panerai, J. C. Ferguson, J. Lachaud, A. Martin, M. J. Gasch, and N. N. Mansour. Micro-tomography based analysis of thermal conductivity, diffusivity and oxidation behavior of rigid and flexible fibrous insulators. *International Journal of Heat and Mass Transfer*, 108:801–811, 2017.

[27] C. Park, G. A. Raiche, D. M. Driver, J. Olejniczak, I. Terrazas-Salinas, T. M. Hightower, and T. Sakai. Comparison of enthalpy determination methods for arc-jet facility. *Journal of thermophysics and heat transfer*, 20(4):672–679, 2006.

[28] D. Prabhu, D. Saunders, C. Tang, I. Terrazas-Salinas, E. Carballo, and D. Driver. CFD Analysis Framework for Arc-Heated Flowfields, II: Shear Testing in Arc-jets at NASA ARC. *AIAA Paper*, 4081, 2009.

[29] A. Sahai, N. N. Mansour, B. Lopez, and M. Panesi. Modeling of high pressure arc-discharge with a fully-implicit Navier–Stokes stabilized finite element flow solver. *Plasma Sources Science and Technology*, 26(5):055012, 2017.

[30] T. Sakai. Computational simulation of high-enthalpy arc heater flows. *Journal of thermophysics and heat transfer*, 21(1):77–85, 2007.

[31] T. Sakai and J. Olejniczak. Navier-Stokes computations for arcjet flows. In *35th AIAA Thermophysics Conference*, page 3014, 2001.

[32] T. Sakai, K. Sawada, and M. Mitsuda. Application of Planck-Rosseland-Gray model for high-enthalpy arc heaters. *Journal of thermophysics and heat transfer*, 15(2):176–183, 2001.

[33] T. Sakai, T. Suzuki, K. Fujita, and T. Ito. Calculation of high-enthalpy aerothermal environment in an arcjet facility. *Journal of thermophysics and heat transfer*, 21(1):249, 2007.

[34] J. B. Scoggins, T. Magin, A. A. Wray, and N. Mansour. Multi-group reductions of lte air plasma radiative transfer in cylindrical geometries. *44th AIAA Thermophysics Conference*, 2013.

[35] J. B. Scoggins and T. E. Magin. Development of Mutation++: Multi-component Thermodynamic and Transport Properties for Ionized Plasmas written in C++. In *11th AIAA/ASME Joint Thermophysics and Heat Transfer Conference*, AIAA Paper 2014-2966, Atlanta, GA, 2014.

[36] R. Smith, D. Wagner, and J. Cunningham. A survey of current and future plasma arc-heated test facilities for aerospace and commercial applications. *AIAA Paper*, 1998.

[37] J. Trelles, E. Pfender, and J. Heberlein. Modelling of the arc reattachment process in plasma torches. *Journal of Physics D: Applied Physics*, 40(18):5635, 2007.

[38] J. P. Trelles. *Finite element modeling of flow instabilities in arc plasma torches*. University of Minnesota, 2007.

[39] J. P. Trelles. Pattern formation and self-organization in plasmas interacting with surfaces. *Journal of Physics D: Applied Physics*, 49(39):393002, 2016.

[40] J. P. Trelles, E. Pfender, and J. Heberlein. Multiscale finite element modeling of arc dynamics in a DC plasma torch. *Plasma chemistry and plasma processing*, 26(6):557–575, 2006.

[41] G. D. Van Albada, B. Van Leer, and W. Roberts. A comparative study of computational methods in cosmic gas dynamics. In *Upwind and high-resolution schemes*, pages 95–103. Springer, 1997.

[42] L. Wang, X. Huang, S. Jia, J. Deng, Z. Qian, Z. Shi, H. Schellenkens, and X. Godechot. 3d numerical simulation of high current vacuum arc in realistic magnetic fields considering anode evaporation. *Journal of Applied Physics*, 117(24):243301, 2015.

[43] L. Wang, X. Huang, X. Zhang, and S. Jia. Modeling and simulation of high-current vacuum arc considering the micro process of anode vapor. *Journal of Physics D: Applied Physics*, 50(9):095203, 2017.

[44] L. Wang, X. Zhou, H. Wang, Z. Qian, S. Jia, D. Yang, and Z. Shi. Anode activity in a high-current vacuum arc: Three-dimensional modeling and simulation. *IEEE Transactions on Plasma Science*, 40(9):2237–2246, 2012.

[45] E. Whiting, L. Yen, J. Arnold, and J. Paterson. NEQAIR96, Nonequilibrium and Equilibrium Radiative Transport and Spectra Program: UserâĂŹs Manual. *NASA RP-1389*, 1996.

[46] W. Winovich and W. C. A. Carlson. The 60-MW Shuttle Interaction Heating Facility. In *25th International Instrumentation Symposium, Anaheim, CA 7-10 May, 1979*, 1979.

[47] M. Winter, D. Prabhu, G. Raiche, I. Terrazas-Salinas, and F. Hui. Emission Spectroscopic Measurements with an Optical Probe in the NASA Ames IHF Arc Jet Facility. In *50th AIAA aerospace sciences meeting including the new horizons forum and aerospace exposition*, page 1016, 01 2012.

[48] A. A. Wray, K. Bensassi, I. N. Kitiashvili, N. N. Mansour, and A. G. Kosovichev. Simulations of Stellar Magnetoconvection using the Radiative MHD CodeStellarBox. *arXiv preprint arXiv:1507.07999*, 2015.